High-Bandwidth AFM-Based Rheology Reveals that Cartilage is Most Sensitive to High Loading Rates at Early Stages of Impairment

Hadi Tavakoli Nia,[†] Iman S. Bozchalooi,[†] Yang Li,[‡] Lin Han,[§] Han-Hwa Hung,[¶] Eliot Frank,[¶] Kamal Youcef-Toumi,[†] Christine Ortiz,[§] and Alan Grodzinsky[†‡¶||*]

[†]Department of Mechanical Engineering, [‡]Department of Biological Engineering, [§]Department of Materials Science and Engineering, [¶]Center for Biomedical Engineering, and [||]Department of Electrical Engineering and Computer Science, Massachusetts Institute of Technology, Cambridge, Massachusetts

ABSTRACT   Utilizing a newly developed atomic-force-microscopy-based wide-frequency rheology system, we measured the dynamic nanomechanical behavior of normal and glycosaminoglycan (GAG)-depleted cartilage, the latter representing matrix degradation that occurs at the earliest stages of osteoarthritis. We observed unique variations in the frequency-dependent stiffness and hydraulic permeability of cartilage in the 1 Hz-to-10 kHz range, a frequency range that is relevant to joint motions from normal ambulation to high-frequency impact loading. Measurement in this frequency range is well beyond the capabilities of typical commercial atomic force microscopes. We showed that the dynamic modulus of cartilage undergoes a dramatic alteration after GAG loss, even with the collagen network still intact: whereas the magnitude of the dynamic modulus decreased two- to threefold at higher frequencies, the peak frequency of the phase angle of the modulus (representing fluid-solid frictional dissipation) increased 15-fold from 55 Hz in normal cartilage to 800 Hz after GAG depletion. These results, based on a fibril-reinforced poroelastic finite-element model, demonstrated that GAG loss caused a dramatic increase in cartilage hydraulic permeability (up to 25-fold), suggesting that early osteoarthritic cartilage is more vulnerable to higher loading rates than to the conventionally studied "loading magnitude". Thus, over the wide frequency range of joint motion during daily activities, hydraulic permeability appears the most sensitive marker of early tissue degradation.

INTRODUCTION

Cartilage, like many soft connective tissues, functions mechanically across a wide spectrum of daily loading frequencies (timescales) (Fig. 1 a), from <1 Hz in slow activities such as walking, to 1000 Hz for high-rate activities such as jumping and impact sports (1–6). Poroelasticity is known to be a major mechanism underlying the macroscale mechanical functions of cartilage, based on theoretical and experimental tests including transient stress relaxation and creep (7–10) and dynamic compression (11). Poroelasticity is manifested via fluid-solid frictional dissipation and intratissue fluid pressurization, which underlie important mechanical functions of cartilage, especially frequency-dependent self-stiffening, energy dissipation, and hydraulic permeation. Recently, nanoscale methodologies have been employed to study cartilage functions under quasistatic and low-frequency loadings (12–14). However, the full frequency spectrum of poroelastic behavior, which is critically important to the understanding of nanoscale dynamic loading, has not been well studied. How does the molecular structure of cartilage provide optimal tissue-level function over the wide spectrum of daily joint motions? And how does impact loading induce molecular-level degradation of the extracellular matrix (ECM), which occurs at the earliest stages of posttraumatic osteoarthritis (15)?

It has been demonstrated previously at the macrotissue scale that cartilage proteoglycans constitute the main resistance to fluid flow under quasistatic and low-frequency loading conditions (12,16,17). Here, we hypothesize that the glycosaminoglycan (GAG) chains of the proteoglycan aggrecan play a dominant role in the high-frequency loading of cartilage as the primary resistance to fluid flow at the nanoscale. Since proteolytic degradation of GAG-containing aggrecan occurs at the earliest stage of osteoarthritis (OA), it could lead to a significant alteration in the ability of cartilage to resist impact compressive loads. The consequences of this GAG loss for the dynamic functioning of cartilage over a wide frequency range have not been illuminated by previous observations regarding quasistatic behavior of the tissue (12,14,18). We have therefore quantified the nanoscale hydraulic permeability of both normal and GAG-depleted cartilage using a novel wide-frequency-range (1 Hz to ~10 kHz) nanorheology system. We show that this nanoscale hydraulic permeability is a sensitive indicator of the loss of cartilage function under high-impact loading frequencies.

MATERIALS AND METHODS

High-frequency AFM-based rheology system

To measure the complex dynamic modulus of cartilage over a wide frequency range (1 Hz to 10 kHz), we developed a high-frequency rheology system coupled to a commercial atomic force microscope (AFM) (MFP-3D, Asylum Research, Santa Barbara, CA). To obtain a vertical displacement on the order of 10 μm in commercial AFMs, a large piezo (on the

a

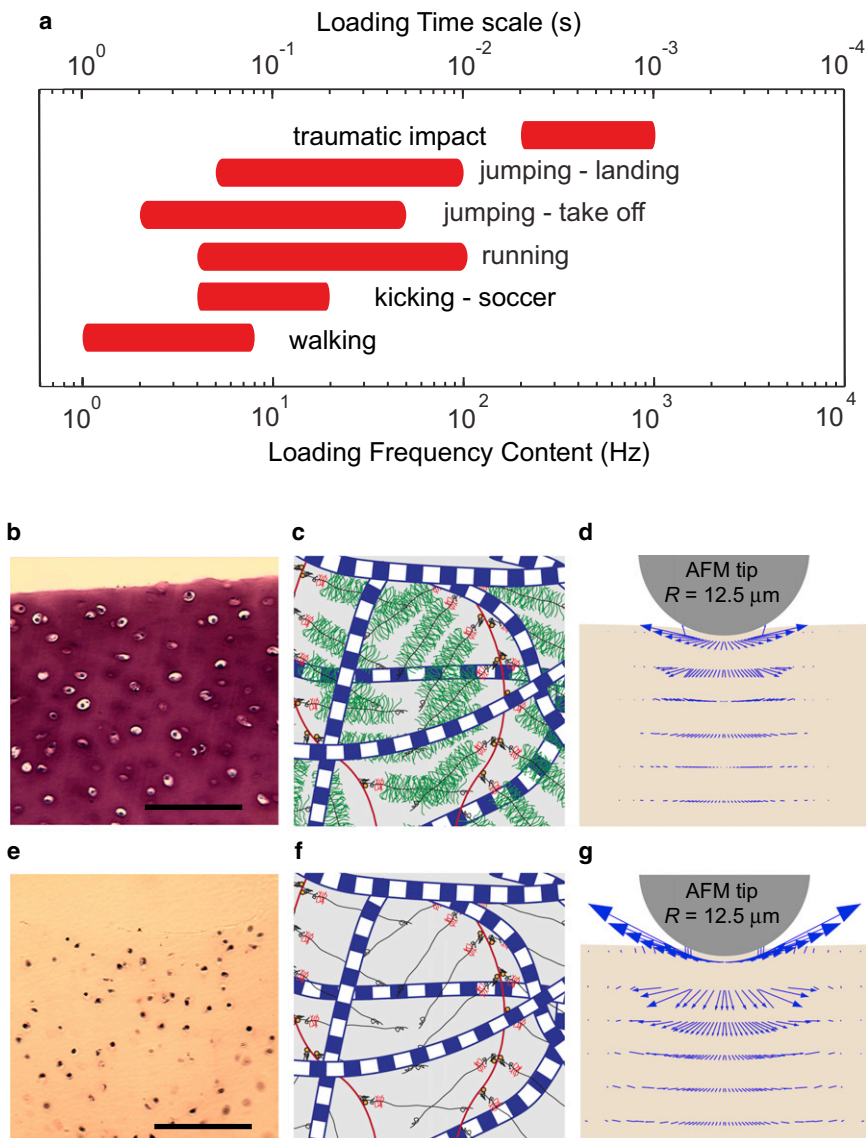Loading Time scale (s)

Loading Frequency Content (Hz)

FIGURE 1 (*a*) The loading-frequency content (timescale) within knee tissues resulting from common physical activities covers a frequency range of 1–1000 Hz (0.001–1 s): walking (1), kicking—soccer (2), running (3), jumping (4), and traumatic impact (5,6). (*b* and *e*) Histologic image of normal (*b*) and GAG-depleted bovine cartilage (*e*) stained with toluidine blue to visualize location and content of GAGs (scale bars, 100 μm). (*c* and *f*) Schematics of the molecular structure of normal (*c*) and GAG-depleted cartilage (*f*) composed mainly of collagen fibers and aggrecan. (*d* and *g*) Schematic of AFM-based dynamic excitation of normal (*d*) and GAG-depleted cartilage (*g*) resulting in intratissue fluid flow velocity as indicated by the arrows (from FEM simulations).

order of centimeters) needs to be chosen. As a result, the resonance frequency/bandwidth of the piezo is low (19), resulting in an upper frequency limit of ~200 Hz (13) or as low as 10 Hz (18) in commercial AFMs (for examples, see Fig. S1 in the Supporting Material). Our approach is to couple a high-frequency actuating system to the commercial AFM. The main component of the system is a small piezo, here called the secondary piezo (Fig. 2 *a*). Unlike the *z*-piezo of the commercial AFM (the primary piezo), the secondary piezo is chosen to be small (2 × 2 × 2 mm) (PL022, Physik Instrumente, Auburn, MA) to maximize the feasible frequency range by pushing the resonance frequency of the combined piezo system to high frequencies. We made the displacement of the secondary piezo load-independent by applying a permanent prestress to the piezo by clamping it between a plate and the substrate (Fig. 2 *a*). The clamp system has its own mechanical resonances, which were diminished by optimizing the plate geometry and material. To have a low weight/stiffness ratio, we fashioned the plate from carbon fiber, with dimension of 0.5 × 5 × 30 mm. We used polystyrene colloidal probe tips with end radius R ~12.5 μm (Polysciences, Warrington, PA) attached to tipless cantilevers with nominal spring constant k ~ 30.0 N/m (Budget Sensors, Sofia, Bulgaria). The colloidal probes were attached to the cantilever by the lift-off process: a dot of glue (M-Bond 610, Structure Probes/SPI Supplies,

West Chester, PA) was placed on a tipless cantilever by making quick contact between the cantilever and a thin layer of glue (1 μl) spread over a 10 × 10-mm mica surface. We then made immediate contact between the tip of the cantilever and a colloid probe resting on a glass slide and waited for 1 min with the cantilever pushing against the colloid. This process was followed by heat curing for 2 h at 150°C.

Loading profile

To fully represent the loading frequencies that human cartilage experiences (Fig. 1 *a*), we chose the indentation loading profile shown in Fig. 2 *b*, a ramp-and-hold preindentation of ~2 μm followed by an oscillatory displacement with a dynamic amplitude of 2 nm. Thus, the dynamic amplitude is less than the dimensions of a single aggrecan (20) or collagen molecule (21). The preindentation is applied using the primary *z*-piezo of the commercial AFM, and the secondary piezo is used to apply the low-amplitude oscillatory displacement over a wide frequency range that is well beyond the capabilities of commercial AFMs. The secondary piezo is activated by an oscillatory frequency sweep signal (DC voltage of 0 V and oscillatory voltage amplitude of 0.5 V), which is generated in LabView
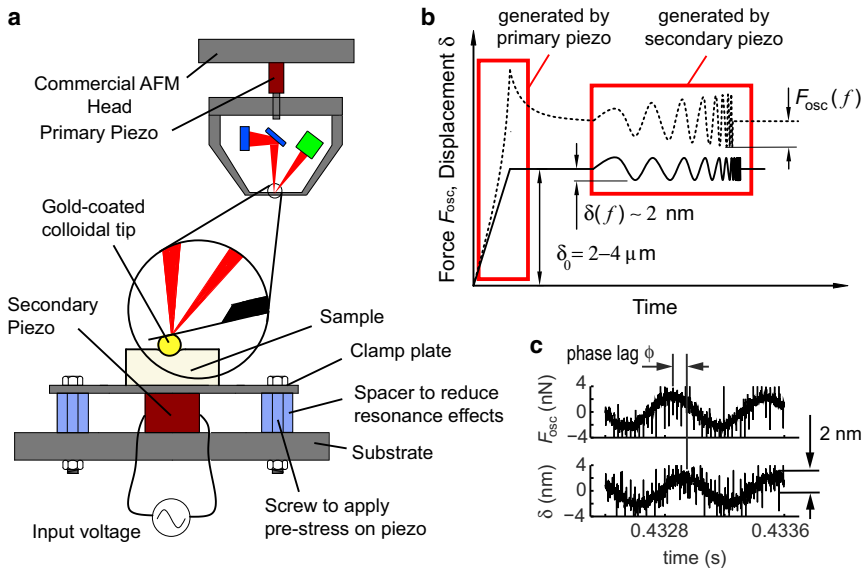
FIGURE 2 (*a*) The commercial AFM is coupled with a high-frequency system to extend the frequency range of dynamic measurement from 1–300 Hz in commercial AFMs to 1 Hz to 10 kHz. (*b*) The dynamic-nanoindentation loading profile is composed of a ramp-and-hold (displacement of ~2 μm, applied by the primary piezo of the commercial AFM) and an oscillatory frequency sweep (sinusoidal displacement amplitude of ~10 nm, applied by the secondary piezo in the newly developed high-frequency system). (*c*) The displacement in the oscillatory loading part is ~2 nm.

(National Instrument, Austin, TX) and amplified by a custom-made power amplifier to supply the required current at high frequencies. The frequency sweep is performed from a start frequency of 1 Hz, with frequency multipliers of 1.2 and with three cycles/frequency (total frequency sweep time ~18 s). The end frequency is 10 kHz. The low number of cycles/frequency is compensated with the low frequency multiplier, which is 1.2. This will result in more than 50 frequencies in the range of 1 Hz to 10 kHz. The sampling rate of the measurement was $f_s = 100$ kHz. The digital-to-analog conversions were performed by data acquisition system NI USB 6351 (National Instrument, Austin, TX). This loading profile was applied to both normal (healthy) (Fig. 1, *b–d*) and GAG-depleted cartilage (Fig. 1, *e–g*), the latter representing one of the earliest events in osteoarthritis (22,23).

Data acquisition and analysis

The z-piezo voltage from the secondary piezo and the deflection voltage from the MFP-3D were measured by the analog-to-digital converter NI USB 6351 and LabView. After the z-piezo and deflection voltages were converted to force, F_{osc}, and displacement, δ, in the time domain, the frequency domain magnitude and phase were calculated from the fast Fourier transform (FFT) of the F_{osc}/δ ratio using MATLAB function etfe. The result was smoothed by applying a Hamming window with a 100-sample size, in which each time series contained ~2×10^6 samples. All data processing was performed using MATLAB (The MathWorks, Natick, MA). The magnitude of the dynamic complex indentation modulus at each frequency was then obtained as (24).

$$|E^*(f)| = \frac{F_{osc}(f)}{\delta(f)} \frac{1}{2(R\delta_0)^{1/2}}, \quad (1)$$

where R is the probe radius. F_{osc}/δ was normalized as above, based on a Taylor series expansion of the Hertz model to account for the spherical probe-tip geometry (24). The phase angle, ϕ, of the dynamic modulus represents the phase of the resulting force, F_{osc}, with respect to the applied displacement, δ (Fig. 2 *c*).

Sample preparation

Eight cartilage cylinders (3 mm in diameter) were harvested from the femoropatellar groove of each of four knee joints from 1- to 2-week-old bovine calves (i.e., four different animals). The cartilage cylinders were harvested within 6 h postmortem and maintained at physiological ionic strength in phosphate buffered saline (PBS) afterward. Two sequential 0.7-mm-thick disks were cut from each cylinder. The intact surface of the first disk included the superficial zone of the cartilage, whereas the second disk consisted of middle-zone cartilage (the superficial zone constitutes the first 100–200 μm in young bovine cartilage (25)). From each joint surface, one set of four superficial/middle-zone disks was kept in PBS with protease inhibitors as normal cartilage, and the mechanical tests were then performed within 6 h after harvesting the samples. The second set was enzymatically GAG-depleted by incubation of the disks for 48 h in PBS containing 0.1 U/ml chondroitinase ABC (26) (Seikagaku Kogyo, Tokyo, Japan). After GAG depletion by this method, the collagen network is still intact (27) (see Fig. S2 for histological images and biochemical measurements of normal and GAG-depleted samples).

Histology

Light microscopy of toluidine-blue-stained disks was used to visualize the spatial distribution of the sulfated GAGs (sGAG) remaining in the disks (28). Axial (vertical) cross sections of normal untreated middle-zone disks showed that sGAG content was spatially uniform throughout the section (Fig. S2 *a*). In normal superficial-zone disks, GAG content decreased gradually from the bottom surface toward the topmost surface, where it is known to have the lowest GAG content of full-thickness cartilage (29) (Fig. S2 *c*). In contrast, after the enzymatic depletion, a spatially uniform loss of GAG was observed throughout disks from both middle-zone and superficial-zone cartilage (Fig. S2, *b* and *d*). For this histological examination, disks were fixed in 10% buffered formalin (Sigma-Aldrich, St. Louis, MO) overnight at 4°C and then dehydrated via a series of graded alcohol incubations followed by xylene. Samples were paraffin-embedded, and 5 μm sections were rehydrated and stained with 0.1% Toluidine blue O (Sigma-Aldrich) in deionized water (pH 7.1).

Biochemical measurements

We used the dimethylmethylene blue assay (30) to obtain a quantitative measure of sGAG content of 0.7-mm-thick disks from the middle zone and the topmost 0.2 mm of the 0.7-mm disks from the superficial zone. Treatment with chondroitinase ABC reduced GAG content by a factor of 8 in the middle-zone disks and by a factor of 3 in the superficial-zone disks

(Fig. S2e). Superficial-zone cartilage has less GAG content (25), and as a result, we observed less relative GAG loss from the superficial zone after enzymatic GAG depletion. These biochemical measurements were performed on all AFM-tested specimens immediately after dynamic indentation tests to most closely reflect GAG content at the time of indentation testing.

Poroelastic finite-element modeling

A fibril-reinforced poroelastic model (31) was implemented in which cartilage is approximated as a composite of an isotropic nonfibrillar matrix (representing the proteoglycan constituents; same element as used in the isotropic model), a fibril network (representing collagen fibrils), and a fluid phase (representing the water/electrolyte solution). We implemented this model by using the soil mechanics capacity of the general-purpose commercial finite-element software ABAQUS (Version 6.9, SIMULIA, Providence, RI). We used axisymmetric poroelastic elements (CAX4P) because of the symmetry of the problem. The AFM probe tip, made of polystyrene, was treated as a rigid solid, since polystyrene ($E \sim 3$ GPa) is much stiffer than cartilage ($E \sim 0.1–0.5$ MPa). For the boundary conditions, we assumed the indenter and the substrate surface to be impermeable to fluid flow and the indenter cartilage-contact region to be frictionless (13). We set the pore pressure to zero at the top surface of the cartilage (excluding the indenter contact surface) and the side surfaces of the cartilage to simulate free draining of the interstitial fluid from the cartilage at those surfaces. The relevant mechanical properties to be estimated are the Young's modulus, E_L, Poisson's ratio, ν, and hydraulic permeability, k, of the nonfibrillar matrix and the Young's modulus of the fibril network. The Young's modulus of the fibrillar network is represented by E_f. As a first approximation, it is assumed that the fibers resist only tension, and the compressive modulus for the fibers is set to zero (31).

Statistics

All the dynamic-modulus measurements were analyzed on the basis of $N = 4$ animals; the value for each animal was calculated as the mean of $n = 4$ disks of normal versus $n = 4$ disks of chondroitinase-treated cartilage from that animal. The value for each disk was calculated as the mean of $m = 4$ indentation sites on each disk. We used the nonparametric Wilcoxon signed rank test (32), since no assumption was made concerning the normality of the data. We used $p < 0.05$ for statistical significance.

RESULTS AND DISCUSSION

GAG depletion markedly alters self-stiffening and energy dissipation

We measured the magnitude of the complex dynamic modulus $|E^*|$ (e.g., Fig. 3 a) and the phase angle, ϕ, of the force with respect to the applied displacement (e.g., Fig. 3 b) for both normal and GAG-depleted cartilage (see Fig. 3, c and d, for the corresponding storage and loss moduli, E' and E'', respectively). $|E^*|$ for normal cartilage decreased to an asymptotic value at low frequencies of $E_L \sim 0.15$ MPa (Fig. 3 a). At high frequencies, $|E^*|$ increased by a factor of 15 to $E_H \sim 2.5$ MPa at $f = 1$ kHz. We observed a similar trend for the GAG-depleted disks, but with overall lower values of $|E^*|$; the low-frequency asymptote was $E_L \sim 0.1$ MPa, whereas at $f = 1$ kHz, $|E^*|$ increased to $E_H \sim 0.8$ MPa, a factor of ~8 higher than E_L. The phase angle, ϕ, measured for normal cartilage peaked

at $f_{peak} = 55$ Hz and tended toward $0°$ at lower and higher frequencies. A similar overall trend was observed for the GAG-depleted cartilage, but the peak frequency shifted dramatically upward to $f_{peak} = 800$ Hz. The important features of the magnitude and phase angle of E^* for GAG-depleted cartilage were found at high frequencies ($f \gg 100$ Hz) beyond the frequency range typically accessible using commercial AFMs. The extended frequency range provided by the newly developed system made the observation of f_{peak} for GAG-depleted cartilage possible. The peak frequency of the phase angle, together with frequency dependence of $|E^*|$, are essential for extracting values of the intrinsic mechanical properties of cartilage by nanoindentation (see below) and for studying the link between these nanoscale mechanical properties and the molecular structure and composition of the ECM.

The protection of chondrocytes from impact loading is associated with the matrix poroelastic mechanisms of self-stiffening and energy dissipation. Self-stiffening, defined here as the increase in dynamic modulus $|E^*|$ with increasing loading frequency (Fig. 3 a, Normal), protects the soft chondrocytes and their pericellular matrix via an increase in the stiffness of the interterritorial matrix (ECM) in response to dynamic loads. Energy dissipation, which is proportional to the tangent of the phase angle, ϕ (Fig. 3 b), involves dispersal of potentially destructive impact energy by poroelastic viscous dissipation. Consistent with our previous study (13), normal cartilage exhibits self-stiffening at the nanoscale, exemplified here by the increase in dynamic modulus from ~0.1 MPa to 3 MPa (Fig. 3 a) over the frequency range 1–1000 Hz, which encompasses most activities of daily life (Fig. 1 a). At high loading rates, such as those of running and jumping, appropriate self-stiffening increases cartilage's ability to bear impact loads. This self-stiffening pattern is accompanied by an optimum frequency for the peak of the phase angle ϕ (~50 Hz for normal cartilage, as measured here). It is important to not that we found that the self-stiffening and dissipative patterns of GAG-depleted cartilage did not occur until much higher frequencies (Fig. 3 b), by more than a decade compared to normal cartilage. As a result, GAG-depleted cartilage suffers a significant loss in its dynamic modulus at high frequencies (up to ~1000 Hz), a finding that to our knowledge has not been reported previously. In addition, the peak in phase angle is shifted from ~50 Hz to ~1000 Hz. Taken together, these results show that early GAG loss from an otherwise normal cartilage matrix results in a tissue that is unable to withstand impact loading, putting the collagen network at risk, as we describe further below.

Hydraulic permeability is a sensitive indicator of GAG loss

By fitting the fibril-reinforced model to the data obtained from normal and GAG-depleted cartilage (Fig. 3, a and b),
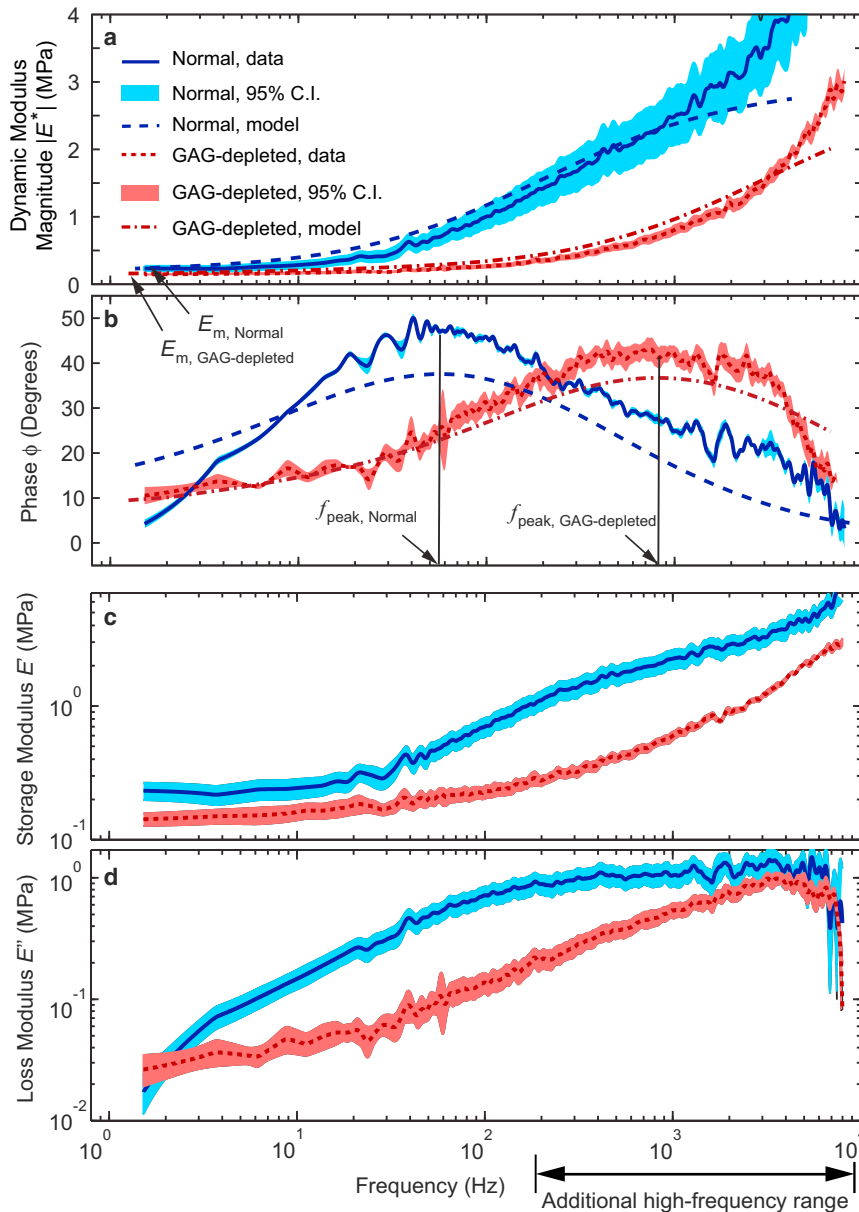
FIGURE 3 (*a* and *b*) The mean value and 95% confidence intervals for the magnitude (*a*) and phase angle (*b*) of the dynamic nanoindentation modulus, $|E^*|$, versus frequency for $n = 4$ cartilage disks harvested from the femoropatellar groove of one bovine calf knee joint with normal (*solid blue line*) and GAG-depleted (*dotted red line*) ECM. The experimental data corresponding to each disk reflect the average of at least $m = 4$ independent indentations at different sites. The FEM simulation results (*dashed lines*), based on a fibril-reinforced model (31), give overall estimates for normal middle-zone cartilage ($E_L = 0.2$ MPa, $E_f = 5$ MPa, $k = 5.4 \times 10^{-15}$ m^4 N^{-1} s^{-1}) and GAG-depleted cartilage ($E_L = 0.15$ MPa, $E_f = 4$ MPa, $k = 1.3 \times 10^{-13}$ m^4 N^{-1} s^{-1}) using a value for Poisson's ratio of $v = 0.1$, which was measured experimentally for cartilage from a bovine calf of the same age (40). (*c* and *d*) The storage modulus, E' (*c*), and loss modulus, E'' (*d*), are shown for both normal and GAG-depleted cartilage. The 95% confidence intervals are computed based on $n = 4$ disks harvested from one typical joint (animal).

the corresponding poroelastic material properties were estimated (see Fig. 4 for averages over all four animals and Fig. S4 for data from the individual animals). For the middle-zone cartilage, where GAG content is normally high and relatively uniform across its depth (Fig. 1 *b*), the equilibrium modulus was $E_{L, normal} = 0.13 \pm 0.042$ MPa, and it decreased by a factor of 1.5 to $E_{L,GAG-depleted} = 0.09 \pm 0.024$ MPa for GAG-depleted tissue (Fig. 4 *c*). However, the hydraulic permeability of these same middle-zone specimens increased by a factor of ~25 from $k_{normal} = 5.4 \times 10^{-15} \pm 2.0 \times 10^{-15}$ m^4/N·s to $k_{GAG-depleted} = 1.3 \times 10^{-13} \pm 0.7 \times 10^{-13}$ m^4/N·s (Fig. 4 *a*). Previous reports using macroscale (33–35) and nanoscale tests (12) have shown that the contribution of aggrecan to the overall equilibrium compressive stiffness of cartilage is comparable to

or greater than the contribution of the collagen network. Therefore, GAG depletion typically decreases the equilibrium modulus by a factor of ~2 or less, which is consistent with the results obtained here. In contrast, the hydraulic permeability of normal cartilage is governed predominantly by GAG chains (36). This is because the equivalent pore size for fluid flow is determined predominantly by the spacing between neighboring GAG chains (~3 nm (20,37)), which is much smaller than the average spacing between collagen fibrils (~100 nm (37)). Thus, depletion of GAG chains can greatly increase the hydraulic permeability, an increase found here to be ~25-fold for middle-zone cartilage.

To further confirm the hypothesis that GAG chains play a major role in the nanoscale poroelastic properties of cartilage, we quantified the effect of GAG depletion on
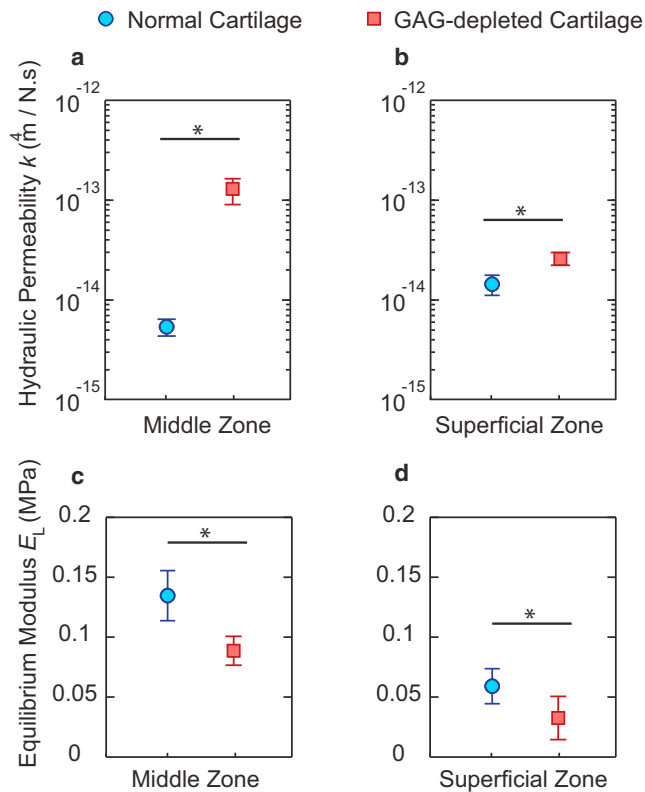
FIGURE 4 The hydraulic permeability, k, of middle-zone (*a*) and superficial-zone cartilage (*b*), and the equilibrium modulus (low-frequency modulus, E_L) of middle-zone (*c*) and superficial-zone cartilage (*d*). All data are presented as the mean $\pm$ SE for $N = 4$ animals, based on a mean of $n = 4$ plugs from each animal. *$p < 0.05$, using the nonparametric Wilcoxon signed rank test. The hydraulic permeability and equilibrium modulus of specimens from individual animals are shown in Fig. S4.

superficial-zone cartilage. In the superficial zone, the overall GAG content is less than in the middle zone (29) and the GAG content is lowest at the uppermost tissue surface (e.g., see histological images in Fig. S2 for normal and GAG-depleted conditions). We observed that after GAG depletion, the equilibrium modulus decreased from $E_{L, \text{normal}} = 0.06 \pm 0.02$ MPa to $E_{L, \text{GAG-depleted}} = 0.04 \pm 0.02$ MPa, and the hydraulic permeability increased from $k_{\text{normal}} = 1.4 \times 10^{-14} \pm 0.6 \times 10^{-14}$ m^4/N·s to $k_{\text{GAG-depleted}} = 2.6 \times 10^{-14} \pm 0.7 \times 10^{-14}$ m^4/N·s (Fig. 4, *b* and *d*). Thus, the hydraulic permeability of superficial-zone cartilage increased by a factor of ~2 after GAG depletion.

We previously showed experimentally and theoretically that the characteristic peak frequency of the phase angle, f_{peak}, is related to the intrinsic material properties of a cartilage sample by the equation

$$f_{\text{peak}} \, \alpha \, \frac{E_L k}{d^2}, \tag{2}$$

where E_L is the equilibrium modulus, k the hydraulic permeability, and d the characteristic contact distance between the tissue and the AFM probe tip (13). Consistent with

Eq. 2, the alteration in hydraulic permeability and equilibrium modulus caused by GAG depletion (Fig. 4) leads to the observed ~15-fold shift in f_{peak} (Fig. 3 *b*).

Length-scale dependence of the peak frequency is an independent measure of GAG depletion

Using a second, independent approach, we further confirmed the hypothesis that Eq. 2 can be used to directly infer the product of hydraulic permeability and equilibrium modulus ($E_L k$) of a cartilage specimen. Here, we measured the variation in f_{peak} as a function of the characteristic contact distance, d, by changing the static offset indentation depth, δ_0, of Fig. 2 *b*. We observed that the relationship between f_{peak} and $1/d^2$ is linear (Fig. 5) for both normal and GAG-depleted cartilage, but with a much larger slope for the GAG-depleted specimens. The consistency of this linear relationship confirms, first, that the frequency-dependent nanomechanics of GAG-depleted cartilage is governed
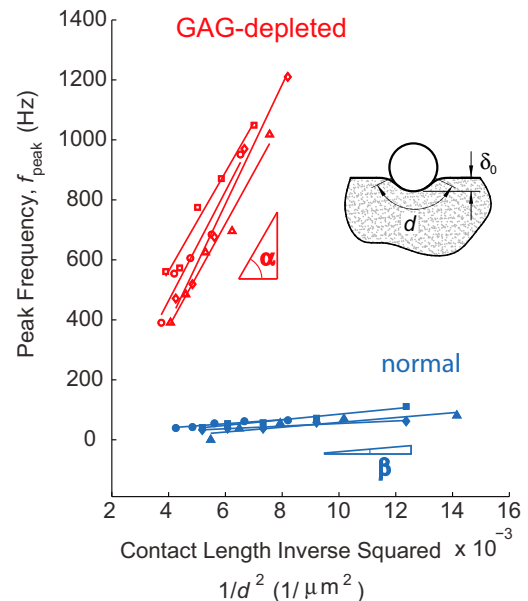

FIGURE 5 The characteristic length-scale dependence of the dynamic modulus was further studied by examining the relationship between the peak frequency of the phase angle, f_{peak}, and the contact distance, d, between the AFM probe tip and cartilage. Using a pair of normal and GAG-depleted disks from adjacent regions of middle-zone cartilage from one animal, the contact distance was changed by increasing the static offset indentation depth, δ_0, and the peak frequency was measured at five different depths δ_0 at each test location for each specimen. The indentation depths, δ_0, varied from 0.9 to 2.8 μm for normal cartilage and from 1.3 to 2.8 μm for GAG-depleted cartilage. The contact distance, d, is calculated from δ_0 via $d = 2R \cos^{-1}((R - \delta_0)/R)$, where $R = 12.5$ μm is the radius of the probe. Linear regression was performed to obtain the best fit, as shown (the lowest value of the goodness of fit, R^2, was 0.9 for all locations). This process was repeated at four different locations on the normal and the GAG-depleted cartilage disks. The average slope of the lines, which is proportional to $E_L k$ (see text after Eq. 2), is measured as $\tan\alpha = (1.65 \pm 0.3) \times 10^5$ Hz·μm^2 and $\tan\beta = (7.12 \pm 2.1) \times 10^3$ Hz·μm^2, (mean $\pm$ SD, $n = 4$) for GAG-depleted and intact cartilage, respectively.

by linear poroelasticity, as previously shown only for normal cartilage (13). Second, the slope of each line represents the $(E_L k)$ product at the precise location of the AFM probe tip during each test. By comparing the experimentally measured slopes for typical normal and GAG-depleted disks (Fig. 5), we observed that the average $(E_L k)$ product for GAG-depleted cartilage was ~23 times greater than the $(E_L k)$ product for normal cartilage, on the same order as the ~15-fold increase obtained from the theoretically predicted values of $(E_L k)$ from our finite-element model (FEM), as well as the shift in f_{peak} observed in Fig. 3 b. This measurement was repeated for most of the disks from other joints, and similar trends were observed.

Hence, the influence of aggrecan-GAG degradation on the nanoscale material properties of cartilage was estimated using Eq. 2. by two independent but self-consistent approaches: 1), the contact distance, d, was held constant for both normal and GAG-depleted cartilage, and the shift in f_{peak} caused by GAG depletion was measured (corresponding to Fig. 3); and 2), the contact distance was experimentally varied for both normal and GAG-depleted cartilage, and the variation of f_{peak} with $1/d^2$ was measured, revealing alterations in the $(E_L k)$ product upon GAG depletion (Fig. 5). Interestingly, Eq. 2 has also been utilized to map the self-stiffening and energy-dissipation properties of cartilage at macroscopic length scales (~1 mm) (38,39). In previous macroscale unconfined dynamic compression tests (38), the length scale chosen (d ~ 3 mm) was 200 times larger than the contact distance of the AFM tip used in this study, d ~ 14 μm. As a result, the measured phase angle of macroscopic unconfined compression tests was shifted to lower frequencies by 5 decades. Equation 2 would therefore predict that f_{peak} would be shifted from ~50 Hz in this study down to ~0.5 mHz; however, this very low macroscale peak frequency was not observable because of low-frequency measurement limitations (38) (see Fig. S5 for this comparison).

Intratissue pressurization is reduced significantly by GAG depletion

Using our fibril-reinforced poroelastic FEM (13), we studied the effects of GAG depletion on the nanoscale intratissue pressure distribution as a function of tissue depth and frequency. The values of E_L and k estimated for normal and GAG-depleted cartilage (Fig. 3 legend) were used in the model to predict the spatial and temporal variations in fluid pressure resulting from dynamic compressive displacement of the AFM probe tip (Fig. 2 b). We found that the significant increase in hydraulic permeability, k, after GAG depletion predicted a greatly reduced intratissue pressurization caused by nanoscale compression (Fig. 6). The fluid pore pressure in normal cartilage is higher by a factor of 5 than that of GAG-depleted cartilage simulated at the peak frequency of the normal cartilage, f_{peak}= 55 Hz. In addition, in normal cartilage, the pressurization penetrates more
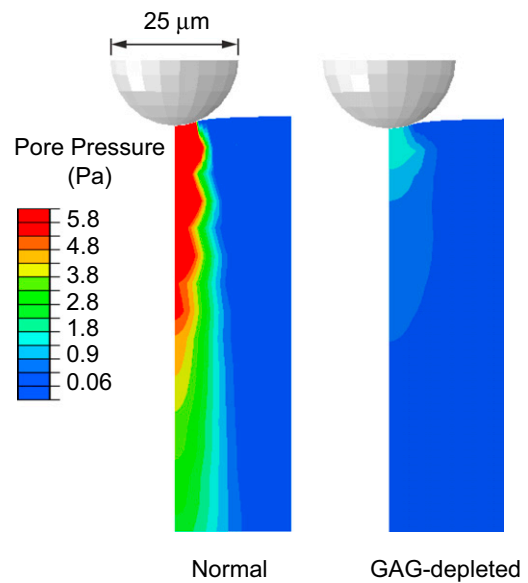

FIGURE 6 Finite-element simulation of the pore pressure at frequency of $f = 55$ Hz in normal ($E_L = 0.1$ MPa, $E_f = 5$ MPa, $k = 5.4 \times 10^{-15}$ m^4 N^{-1} s^{-1}, $v = 0.1$) and GAG-depleted cartilage ($E_L = 0.08$ MPa, $E_f = 4$ MPa, $k = 1.3 \times 10^{-13}$ m^4 N^{-1} s^{-1}, $v = 0.1$) confirms the effect of GAG depletion on fluid pressurization in dynamic loading, which consequently alters the nanoscale dynamic functions of cartilage, such as self-stiffening and energy dissipation. The pressure profile shown for each condition is the maximum amplitude of the pore pressure versus depth at the frequency of $f = 55$ Hz, the frequency at which the phase angle, ϕ, measured for the normal cartilage peaks.

deeply into the matrix and involves a larger volume of the matrix engaged in dissipation and self-stiffening at high loading frequencies. In contrast, in GAG-depleted cartilage, not only is the pore pressure reduced (Fig. 6), but because of the larger matrix pore size, the fluid velocity is higher at the location of loading (Figs. 1 g and 6). GAG loss thereby reduces the self-stiffening and energy-dissipation properties of the ECM, and consequently, the chondrocytes may be more prone to damage caused by impact loads during the earliest stages of OA. In addition to these dissipative features, fluid pressure and flow velocity are also known to play significant roles in modulation of the cell-matrix biosynthesis (40). Thus, the ability of chondrocytes to respond to the proanabolic signals associated with moderate, low-frequency dynamic compression (41) could be significantly compromised by the consequences of high-frequency impact loading.

We believe that the information obtained from this study can aid in the fundamental understanding of the mechanisms involved in pathological processes and tissue regeneration of biological tissues at the molecular (42,43), cellular (44,45), and ECM levels (14,46–48). For example, in the ECM of tumors, the interstitial fluid pressurization compresses the blood vessels, which results in reduction of blood flow (46). Reduction of blood flow, accompanied by hypoxia, in turn promotes tumor progression. This study

thus may provide direct molecular-level insight into similar applications in the mechanopathology of tumors, where the fluid-solid interaction plays a critical role. Our wide-frequency approach in determining the nanoscale hydraulic permeability may also provide insight into the transport problems in hydrogels (49) and soft hydrated tissues with a wide range of poroelastic material properties.

CONCLUSION

In this study, we measured the high-frequency dynamic nanomechanics of normal and GAG-depleted cartilage, the latter representing a critical aspect of matrix degradation in the earliest stages of OA. The high-frequency measurements, which simulate loading rates during activities such as running and jumping, were made possible by developing a high-frequency nanorheology system coupled to commercial AFMs. Equipped with this system, we were able to investigate molecular-level fluid-solid interactions which manifest predominantly at higher frequencies. We quantified alterations in nanoscale poroelastic properties of cartilage caused by GAG depletion using a FEM-based fibril-reinforced poroelastic model. First, we showed that the nanoscale hydraulic permeability of cartilage is a more sensitive differentiator of early-OA-like matrix degradation compared to the nanoscale equilibrium modulus: GAG depletion increased the nanoscale hydraulic permeability of middle-zone cartilage by a factor of ~25, whereas the equilibrium modulus decreased by just 40%. Second, we demonstrated that GAG chains play a dominant role in the nanoscale resistance of cartilage matrix to fluid flow and intratissue pressurization, which, at the macroscale (50), is known to protect the tissue from high-loading-rate activities. At early stages of OA, during which GAG chains are being depleted but the collagen network may still be completely intact, the collagen network becomes more prone to damage caused by high-rate impact loading. Thus, we hypothesize that early-stage GAG-depleted cartilage is more susceptible to loading rate than the more conventionally studied load magnitude.

SUPPORTING MATERIAL

REFERNCES

1. Cross, R. 1999. Standing, walking, running, and jumping on a force plate. *Am. J. Phys.* 67:304–309.

2. Tanaka, Y., M. Shiokawa, …, T. Tsuji. 2006. Manipulability analysis of kicking motion in soccer based on human physical properties. *IEEE Trans. Syst. Man Cybern.* 1:68–73.

3. Dickinson, J. A., S. D. Cook, and T. M. Leinhardt. 1985. The measurement of shock waves following heel strike while running. *J. Biomech.* 18:415–422.

4. Richards, D. P., S. V. Ajemian, …, R. F. Zernicke. 1996. Knee joint dynamics predict patellar tendinitis in elite volleyball players. *Am. J. Sports Med.* 24:676–683.

5. Heiner, A. D., J. A. Martin, …, T. D. Brown. 2012. Frequency content of cartilage impact force signal reflects acute histologic structural damage. *Cartilage.* 3:314–322.

6. Hoshino, A., and W. A. Wallace. 1987. Impact-absorbing properties of the human knee. *J. Bone Joint Surg. Br.* 69:807–811.

7. Hu, Y., E. P. Chan, …, Z. Suo. 2011. Poroelastic relaxation indentation of thin layers of gels. *J. Appl. Phys.* 110:086103–086105.

8. Mow, V. C., S. C. Kuei, …, C. G. Armstrong. 1980. Biphasic creep and stress relaxation of articular cartilage in compression? Theory and experiments. *J. Biomech. Eng.* 102:73–84.

9. Mak, A. F., W. M. Lai, and V. C. Mow. 1987. Biphasic indentation of articular cartilage—I. Theoretical analysis. *J. Biomech.* 20:703–714.

10. Buckley, M. R., J. P. Gleghorn, …, I. Cohen. 2008. Mapping the depth dependence of shear properties in articular cartilage. *J. Biomech.* 41:2430–2437.

11. Frank, E. H., and A. J. Grodzinsky. 1987. Cartilage electromechanics—II. A continuum model of cartilage electrokinetics and correlation with experiments. *J. Biomech.* 20:629–639.

12. Han, L., E. H. Frank, …, C. Ortiz. 2011. Time-dependent nanomechanics of cartilage. *Biophys. J.* 100:1846–1854.

13. Nia, H. T., L. Han, …, A. Grodzinsky. 2011. Poroelasticity of cartilage at the nanoscale. *Biophys. J.* 101:2304–2313.

14. Stolz, M., R. Gottardi, …, U. Aebi. 2009. Early detection of aging cartilage and osteoarthritis in mice and patient samples using atomic force microscopy. *Nat. Nanotechnol.* 4:186–192.

15. Anderson, D. D., S. Chubinskaya, …, J. A. Buckwalter. 2011. Post-traumatic osteoarthritis: improved understanding and opportunities for early intervention. *J. Orthop. Res.* 29:802–809.

16. Bonassar, L. J., E. H. Frank, …, A. J. Grodzinsky. 1995. Changes in cartilage composition and physical properties due to stromelysin degradation. *Arthritis Rheum.* 38:173–183.

17. Maroudas, A. 1975. Biophysical chemistry of cartilaginous tissues with special reference to solute and fluid transport. *Biorheology.* 12:233–248.

18. Desrochers, J., M. W. Amrein, and J. R. Matyas. 2012. Viscoelasticity of the articular cartilage surface in early osteoarthritis. *Osteoarthritis Cartilage.* 20:413–421.

19. Manalis, S. R., S. C. Minne, and C. F. Quate. 1996. Atomic force microscopy for high speed imaging using cantilevers with an integrated actuator and sensor. *Appl. Phys. Lett.* 68:871–873.

20. Ng, L., A. J. Grodzinsky, …, C. Ortiz. 2003. Individual cartilage aggrecan macromolecules and their constituent glycosaminoglycans visualized via atomic force microscopy. *J. Struct. Biol.* 143:242–257.

21. Jeffery, A. K., G. W. Blunn, …, G. Bentley. 1991. Three-dimensional collagen architecture in bovine articular cartilage. *J. Bone Joint Surg. Br.* 73:795–801.

22. Sui, Y., J. H. Lee, …, A. J. Grodzinsky. 2009. Mechanical injury potentiates proteoglycan catabolism induced by interleukin-6 with soluble interleukin-6 receptor and tumor necrosis factor alpha in immature bovine and adult human articular cartilage. *Arthritis Rheum.* 60:2985–2996.

23. Guilak, F., A. Ratcliffe, …, V. C. Mow. 1994. Mechanical and biochemical changes in the superficial zone of articular cartilage in canine experimental osteoarthritis. *J. Orthop. Res.* 12:474–484.

24. Mahaffy, R. E., S. Park, …, C. K. Shih. 2004. Quantitative analysis of the viscoelastic properties of thin regions of fibroblasts using atomic force microscopy. *Biophys. J.* 86:1777–1793.

25. Klein, T. J., M. Chaudhry, …, R. L. Sah. 2007. Depth-dependent biomechanical and biochemical properties of fetal, newborn, and tissue-engineered articular cartilage. *J. Biomech.* 40:182–190.

26. Asanbaeva, A., K. Masuda, …, R. L. Sah. 2007. Mechanisms of cartilage growth: modulation of balance between proteoglycan and collagen in vitro using chondroitinase ABC. *Arthritis Rheum.* 56:188–198.

27. Billinghurst, R. C., W. Wu, …, A. R. Poole. 2000. Comparison of the degradation of type II collagen and proteoglycan in nasal and articular cartilages induced by interleukin-1 and the selective inhibition of type II collagen cleavage by collagenase. *Arthritis Rheum.* 43:664–672.

28. Karsdal, M. A., E. U. Sumer, …, B. C. Sondergaard. 2007. Induction of increased cAMP levels in articular chondrocytes blocks matrix metalloproteinase-mediated cartilage degradation, but not aggrecanase-mediated cartilage degradation. *Arthritis Rheum.* 56:1549–1558.

29. Xia, Y., S. K. Zheng, and A. Bidthanapally. 2008. Depth-dependent profiles of glycosaminoglycans in articular cartilage by microMRI and histochemistry. *J. Magn. Reson. Imaging.* 28:151–157.

30. Farndale, R. W., D. J. Buttle, and A. J. Barrett. 1986. Improved quantitation and discrimination of sulphated glycosaminoglycans by use of dimethylmethylene blue. *Biochim. Biophys. Acta.* 883:173–177.

31. Soulhat, J., M. D. Buschmann, and A. Shirazi-Adl. 1999. A fibril-network-reinforced biphasic model of cartilage in unconfined compression. *J. Biomech. Eng.* 121:340–347.

32. Conover, W., and R. L. Iman. 1981. Rank transformations as a bridge between parametric and nonparametric statistics. *Am. Stat.* 35:124–129.

33. Williamson, A. K., A. C. Chen, and R. L. Sah. 2001. Compressive properties and function-composition relationships of developing bovine articular cartilage. *J. Orthop. Res.* 19:1113–1121.

34. Maroudas, A. 1980. Physical chemistry of articular cartilage and the intervertebral disc. *In* The Joints and Synovial Fluid. L. Sokoloff, editor. Academic Press, New York. 239–291.

35. Eisenberg, S. R., and A. J. Grodzinsky. 1985. Swelling of articular cartilage and other connective tissues: electromechanochemical forces. *J. Orthop. Res.* 3:148–159.

36. Maroudas, A., J. Mizrahi, …, I. Ziv. 1987. Swelling pressure in cartilage. *Adv. Microcirc.* 13:203–212.

37. Roughley, P. J., and E. R. Lee. 1994. Cartilage proteoglycans: structure and potential functions. *Microsc. Res. Tech.* 28:385–397.

38. Kim, Y. J., L. J. Bonassar, and A. J. Grodzinsky. 1995. The role of cartilage streaming potential, fluid flow and pressure in the stimulation of chondrocyte biosynthesis during dynamic compression. *J. Biomech.* 28:1055–1066.

39. Frank, E. H., and A. J. Grodzinsky. 1987. Cartilage electromechanics—I. Electrokinetic transduction and the effects of electrolyte pH and ionic strength. *J. Biomech.* 20:615–627.

40. Buschmann, M. D., Y.-J. Kim, …, A. J. Grodzinsky. 1999. Stimulation of aggrecan synthesis in cartilage explants by cyclic loading is localized to regions of high interstitial fluid flow. *Arch. Biochem. Biophys.* 366:1–7.

41. Grodzinsky, A. J., M. E. Levenston, …, E. H. Frank. 2000. Cartilage tissue remodeling in response to mechanical forces. *Annu. Rev. Biomed. Eng.* 2:691–713.

42. Han, L., D. Dean, …, A. J. Grodzinsky. 2007. Lateral nanomechanics of cartilage aggrecan macromolecules. *Biophys. J.* 92:1384–1398.

43. Dean, D., L. Han, …, C. Ortiz. 2006. Compressive nanomechanics of opposing aggrecan macromolecules. *J. Biomech.* 39:2555–2565.

44. Charras, G. T., J. C. Yarrow, …, T. J. Mitchison. 2005. Non-equilibration of hydrostatic pressure in blebbing cells. *Nature.* 435:365–369.

45. Lee, B. B., L. Han, …, A. J. Grodzinsky. 2010. Dynamic mechanical properties of the tissue-engineered matrix associated with individual chondrocytes. *J. Biomech.* 43:469–476.

46. Stylianopoulos, T., J. D. Martin, …, R. K. Jain. 2012. Causes, consequences, and remedies for growth-induced solid stress in murine and human tumors. *Proc. Natl. Acad. Sci. USA.* 109:15101–15108.

47. Jiao, T., A. Farran, …, R. J. Clifton. 2009. High frequency measurements of viscoelastic properties of hydrogels for vocal fold regeneration. *Exp. Mech.* 49:235–246.

48. Donnelly, E., R. M. Williams, …, M. C. H. van der Meulen. 2006. Quasistatic and dynamic nanomechanical properties of cancellous bone tissue relate to collagen content and organization. *J. Mater. Res.* 21:2106–2117.

49. Kalcioglu, Z. I., R. Mahmoodian, …, K. J. Van Vliet. 2012. From macro- to microscale poroelastic characterization of polymeric hydrogels via indentation. *Soft Matter.* 8:3393–3398.

50. Soltz, M. A., and G. A. Ateshian. 1998. Experimental verification and theoretical prediction of cartilage interstitial fluid pressurization at an impermeable contact interface in confined compression. *J. Biomech.* 31:927–934.

51. Clarke, R. J., S. Cox, …, O. Jensen. 2005. The drag on a microcantilever oscillating near a wall. *J. Fluid Mech.* 545:397–426.

52. Benmouna, F., and D. Johannsmann. 2002. Hydrodynamic interaction of AFM cantilevers with solid walls: an investigation based on AFM noise analysis. *Eur. Phys. J. E. Soft Matter.* 9:435–441.

53. Craig, V. S. J., and C. Neto. 2001. In situ calibration of colloid probe cantilevers in force microscopy: hydrodynamic drag on a sphere approaching a wall. *Langmuir.* 17:6018–6022.

54. Ljung, L. 1999. System Identification: Theory for the User. Prentice-Hall, Upper Saddle River, NJ.